



Available online at www.keaipublishing.com/en/journals/journal-of-magnesium-and-alloys/

ScienceDirect

Journal of Magnesium and Alloys 13 (2025) 3673-3688



www.elsevier.com/locate/jma

Full Length Article

Excellent strength-ductility synergy property of wire-arc additively manufactured Mg-Gd-Y-Zr alloy investigated by heat treatment

Jiamin Li^a, Meng Huang^a, Juan Hou^{a,*}, Xingbin Wang^a, Gaopeng Xu^a, Yi Yang^a, Ning Mo^b, Yun Shi^c, Laichang Zhang^d, Weineng Tang^{b,*}

^a Interdisciplinary Centre for Additive Manufacturing (ICAM), School of Materials and Chemistry, University of Shanghai for Science and Technology, Shanghai 200093, China

^bMg & Mg Alloy Research Institute, Technology Center, Baosteel Metal Co., Ltd., China Baowu Steel Group Corporation, Shanghai 200940, China ^c Shanghai Aerospace Equipment Manufacturer Co., Ltd., Shanghai 201100, China

d Centre for Advanced Materials and Manufacturing, School of Engineering, Edith Cowan University, 270 Joondalup Drive, Joondalup, Perth, 6027, WA, Australia

Received 2 January 2025; received in revised form 14 March 2025; accepted 31 March 2025 Available online 10 June 2025

Abstract

In this work, the GW63K (Mg-6.54Gd-3.93Y-0.41Zr, wt.%) alloy wire was utilized as the feedstock material and the thin-walled component was fabricated using wire-arc additive manufacturing technology (WAAM). The microstructural evolution during deposition and subsequent heat treatment was explained through multi-scale microstructural characterization techniques, and the impact of heat treatment on the strength-ductility synergy of the deposited alloy was systematically compared. The results showed that the microstructure of the deposited sample was mainly composed of fine equiaxed α -Mg grains and Mg₂₄(Gd,Y)₅ phase. The optimized solution heat treatment (450 °C × 2 h) had little effect on the grain size, but can effectively reduce the Mg₂₄(Gd,Y)₅ eutectic phase on the grain boundary, resulting in a significant increase in elongation from 13.7% to 26.6%. After peak-aging treatment, the strength of the GW63K alloy increased to 370 MPa, which was significantly higher than the as-built state (267 MPa). The superior strength in this study is attributed to the refinement strengthening imparted by the fine microstructure inherited in the as-built GW63K alloy, as well as the precipitation strengthening due to the formation of dense β ' precipitates with a pronounced plate-like aspect ratio.

© 2025 Chongqing University. Publishing services provided by Elsevier B.V. on behalf of KeAi Communications Co. Ltd. This is an open access article under the CC BY-NC-ND license (http://creativecommons.org/licenses/by-nc-nd/4.0/)

Keywords: Mg-Gd-Y-Zr alloy; Wire-arc additive manufacturing; Microstructure; Heat treatment; Strength-ductility synergy.

1. Introduction

Magnesium rare-earth (Mg-RE) alloys are increasingly recognized for their potential in lightweight applications across the aerospace and transportation sectors. This is primarily due to their inherent characteristics of low density, high specific strength, and enhanced creep resistance [1–7]. To date, gadolinium (Gd) and yttrium (Y) are the most widely employed rare earth elements due to their significant contribu-

E-mail addresses: hou18217727686@163.com (J. Hou), tangweineng@baosteel.com (W. Tang).

tion to precipitation strengthening [8–10]. Binary Mg-Gd and Mg-Y alloys exhibit phase diagrams where the maximum solubility of Gd and Y in the solid Mg matrix is 23.7 wt.% at 548 °C and 13.9 wt.% at 574 °C, respectively [11]. High-density nanoscale β' prismatic precipitates are a critical factor in achieving substantial precipitation strengthening, as these precipitates effectively hinder the movement of basal dislocations and twins [12,13]. In addition, zirconium (Zr) is commonly incorporated as a grain refiner to achieve substantial grain refinement and enhanced strengthening effects [14–16].

Historically, Mg-RE alloys have predominantly been produced using traditional casting techniques, such as sand casting [17] or die casting [18], which often lead to the formation of undesirable casting defects and a coarsened microstruc-

[☆] Peer review under the responsibility of Chongqing University.

^{*} Corresponding authors.

ture [19–22]. With the development of additive manufacturing (AM) technology and the demand for lightweight and high-strength components, people are increasingly interested in using wire arc additive manufacturing (WAAM) to produce high-strength Mg alloy components [23–26]. However, previous research has largely focused on the WAAM process of AZ-series Mg-Al alloys, primarily because wire feedstock for these alloys is more readily available [27–29]. At present, with the improvement of Mg-RE alloy wire processing technology, WAAM of Mg-RE alloy has attracted widespread attention.

Currently, there are still very limited reports on additive manufacturing of Mg-RE alloys, and due to the imperfect heat treatment method, the excellent properties of Mg-RE alloys have not yet been brought into play. Specifically, Tong et al. [30] examined how the microstructural evolution and mechanical characteristics were affected by the in-situ heat treatment that is a part of the tungsten inert gas wire arc additive manufacturing (TIG-WAAM) preparation process for WE43 (Mg-4.15Y-2.13Nd-1.12Gd-0.55Zr, wt.%). Li et al. [31] explored the microstructural evolution in GWZ421K (Mg-4.4Gd-2.2Y-1.0Zn-0.5Zr, wt.%) thin walls fabricated by WAAM by manipulating the precipitates through heat treatment processing. Cao et al. [32] fabricated single-pass multilayer deposits of GWZ1031K (Mg-10Gd-3Y-1Zn-0.5Zr, wt.%) using the TIG-WAAM technique. Their study systematically examined the microstructural evolution during both the TIG-WAAM process and the subsequent heat treatment. It is worth noting that although both WE43, GWZ421K, and GWZ103K alloys have achieved significant strengths of >285 MPa, there is still a big gap compared to the same grade alloys of traditional forging.

Inspired by the above breakthrough findings, this study systematically studied the microstructural evolution and mechanical properties of GW63K alloy prepared by WAAM process and heat treatment using optimal parameters for better performance. Furthermore, using advanced characterization techniques, the effects of solid solution treatment and aging on the precipitation phases, grain size, and tensile properties were thoroughly analyzed. This study explored a Mg-Gd-Y series magnesium alloy with superior strength-ductility synergy, which provides new insights for alloy design and performance regulation for the future preparation of large magnesium alloy components with complex structures.

2. Materials and experimental

2.1. Material preparation and WAAM process

In this work, the GW63K (Mg-6.54Gd-3.93Y-0.41Zr, wt.%) alloy wire with a diameter of 1.6 mm was used as the feedstock. The radial and axial cross sections of the feedstock are visible in the SEM images shown in Fig. 1(a) and (b). A GWZ941K magnesium alloy extruded plate, measuring 300 mm \times 200 mm \times 50 mm, was used as the substrate. The substrate was polished with 800# SiC sandpaper and cleaned with ethanol before WAAM deposition to remove any impurities, and then preheated to 200 °C by a heating platform to promote the bonding between the deposited parts and the substrate. The WAAM setup primarily consists of a Fronius CMT Advanced 4000R welding unit equipped with a wire feeding mechanism, an ABB six-axis industrial robot with a welding torch, an argon gas delivery system, and a robot controller. We conducted a large number of single-pass deposition experiments. Based on preliminary experimental results, the WAAM process parameters are detailly listed in Table 1. It was necessary to establish a common reference coordinate system before deposition (Fig. 1c).

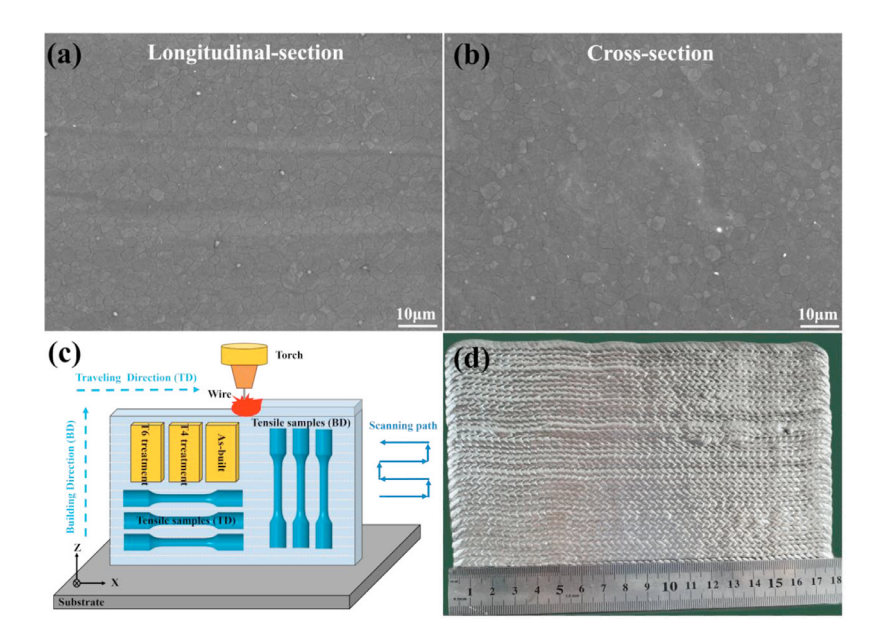


Fig. 1. SEM images of the GW63K alloy wire on: (a) longitudinal-section; (b) cross-section. (c) Schematic illustration of the WAAM process and extraction locations of the samples taken for characterization and (d) macro-morphology of thin-wall WAAM processed component.

Table 1 Deposition parameters in the WAAM process.

Process parameters	Details	Value
Deposition power	Current	110 A
	Arc voltage	12 V
Speed	Feeding speed	10 m/min
	Welding speed	9 m/min
Distance	Arc length	0.012 m
Time	Inter-pass time	60 s
Flow rate (argon)	Trailing shield	20 L/min

Table 2 Chemical compositions (wt.%) of the feedstock and as-built components.

Alloys	Mg	Gd	Y	Zr	
Wire	Bal.	6.54	3.93	0.41	
As-built	Bal.	6.44	3.27	0.40	

The wire was deposited layer by layer on the substrate using a unidirectional reciprocating strategy. Fig. 1(d) shows the GW63K alloy thin-walled sample with the dimensions of $150~\text{mm} \times 70~\text{mm} \times 15~\text{mm}$ (length \times height \times width) and the sampling position. In this system, the X-axis corresponds to the traveling direction (TD) of the welding gun, the Z-axis represents the building direction (BD), and the Y-axis denotes the normal direction (ND). As shown in Table 2, the elemental composition of the wire and the as-built GW63K deposited bulk was determined using inductively coupled plasma atomic emission spectrometry (ICP-AES, Thermo iCAP 7000, USA).

2.2. Heat treatment

Given the substantial solid solution strengthening and agehardening potential of Mg-Y-Zr alloys, implementing an effective heat treatment process for WAAM-fabricated GW63K alloy samples is essential to achieve superior application properties. To better understanding the phase transformation through heat treatment, Fig. 2 presents the non-equilibrium phase diagram of the Mg-6.44Gd-3.27Y-0.40Zr alloy, derived from the chemical composition of the WAAM-GW63K sample. This phase diagram was developed using the Scheil-Gulliver solidification model and calculated with Thermodynamics JMatPro® software. As can be seen from Fig. 2, the Mg₅Gd phase and Mg₂₄Y₅ phase can be fully decomposed into the magnesium matrix at 310.2 °C and 278.4 °C, respectively, but the influence of environmental and time factors must be considered in actual experiments. A solid solution temperature of 400-525 °C was thus set based on the thermodynamic calculation results, and water cooling (referred as T4 treatment) was performed after 1-2 h of heat preservation. According to early research results, the aging temperature of Mg-Gd-Y-Zr alloy is set at 200 °C. In conclusion, the samples in this study underwent solution treatment, followed by aging at 200 °C for durations ranging from 6 to 144 h, and were subsequently air-cooled (referred as T6 treatment).

2.3. Microstructure characterization

The sample locations for microstructural characterization are shown in Fig. 1(c). Metallographic specimens were sectioned from the thin-wall structure along the deposition direction using wire electrical discharge machining (EDM) to facilitate microstructural observation both before and after heat treatment. The location of the characterized sample is designated as the XZ plane. Optical microstructural observations are carried out on a KEYENCE VHT-7000 N optical microscope (OM). A ZEISS Sigma 500 Scanning Electron Microscope (SEM) equipped with an AMETEK EDAX Octane Elite system (including an energy-dispersive spectrometer (EDS) and an electron backscatter diffraction (EBSD) system) was used to investigate the microstructures, elemental distributions, grain size and crystal orientation. The surface morphology of the sample was observed in BSE mode, with a scanning voltage of 20 kV and an aperture of 120 µm. The step size for EBSD scanning was 1.0 µm, and the EBSD data was then analyzed by TSL OIM Analysis 8.0 software. Phase identification was carried out by a Bruker D8 Advance diffractometer (XRD) using a Cu Kα source at 40 kV and 300 mA, with a scanning rate of 2°/min over a range of 20° to 80°. A ThermoFisher Talos F200X transmission electron microscopy (TEM) was used to further characterize the second phase and the nanoscale precipitation phase. The sample was processed into a thin slice with a thickness of 1 mm, and then ground with sandpaper to reduce the thickness of the slice to 100 µm. Then, a circular sample with a diameter of 3 mm was prepared using a punching device. Finally, a GATAN PIPS II ion thinning instrument was used to perform thinning at $\pm 5^{\circ}$ and 4 keV until a through hole was formed in the sample, thereby obtaining a thin area.

For OM, SEM, EDS and XRD characterization, the samples were prepared by mechanical grinding/ polishing, followed by etching in 4 vol% nitric alcohol. EBSD samples were prepared by mechanical grinding, followed by electropolish with 10 vol% perchloric acid and 90 vol% ethanol mixed solution, under working voltage of 15 V, current of 0.5 A and polishing time of 30 s.

2.4. Mechanical properties analysis

Tensile specimens were extracted from the thin-walled wall by wire EDM (Fig. 1(c)). The tensile test was conducted on a SUNS UTM2000 universal testing machine in accordance with ASTM E8/E8M standard. The tensile samples of all groups were tested at least 3 times at a constant speed of 1 mm/min to ensure the stability of the data. After the tensile test, the fracture morphology was observed by SEM. The Vickers hardness measurements were conducted using a Buehler VH-1102 microhardness tester, applying a load of 100 g with a dwell time of 10 s. The sample was tested at 50 locations along the building direction (BD), with a step size of 1 mm, to obtain the average microhardness value.

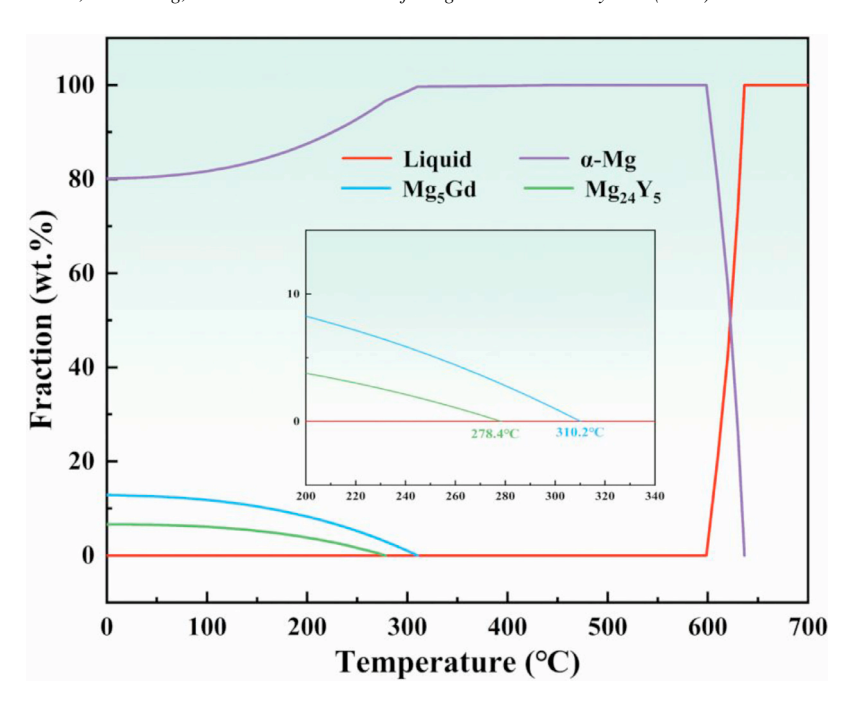


Fig. 2. The non-equilibrium phase diagram of Mg-6.44Gd-3.27Y-0.40Zr (wt.%) alloy calculated using JMatPro® software.

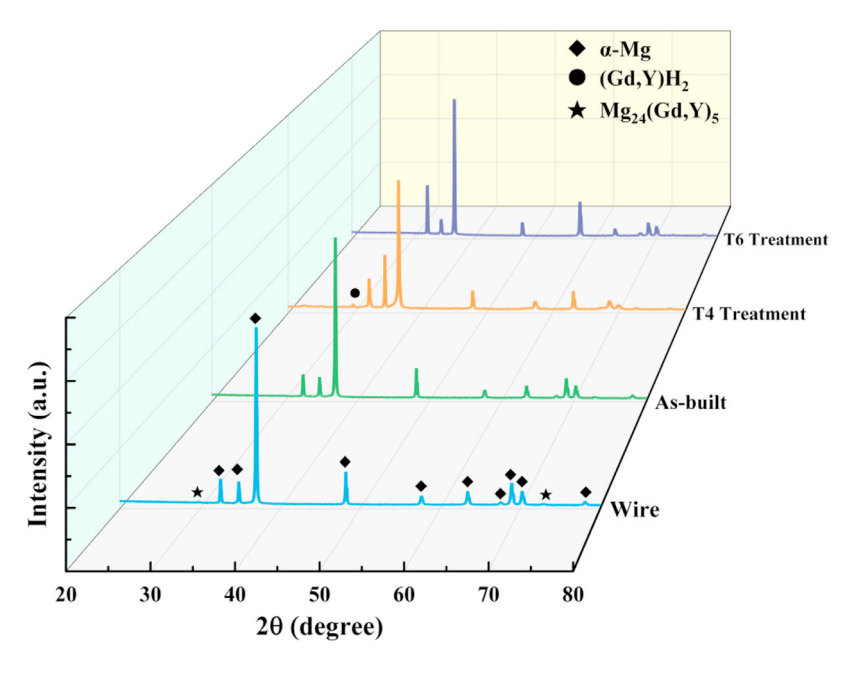


Fig. 3. XRD patterns of WAAM-GW63K at four states.

3. Results

3.1. Phase analysis

XRD analysis of the wire, as-built and heat-treatment samples of GW63K is shown in Fig. 3. The wire and as-built sample mainly contain α -Mg matrix and Mg₂₄(Gd,Y)₅ phase (PDF#31–0827). Although the Mg₅Gd phase is shown in the non-equilibrium phase diagram calculated by JMatPro® software, its diffraction peak is not detected due to the relatively low content. The diffraction peaks exhibited no significant

changes following the T4 and T6 heat treatments, which was attributed to the tiny size, low content and insufficient accuracy of XRD analysis on aged precipitates. However, after T4 heat treatment, obvious (Gd, Y) H₂ phase (PDF#89–4063) diffraction peaks appeared. This is mainly because during the solution treatment stage, Gd and Y elements are evenly distributed in the magnesium matrix due to their high solid solubility; in the subsequent aging treatment, rare earth elements are segregated by diffusion. Zr, as a grain refiner, not only inhibits grain coarsening, but also provides nucleation sites for local enrichment of rare earth elements. At this time, due to

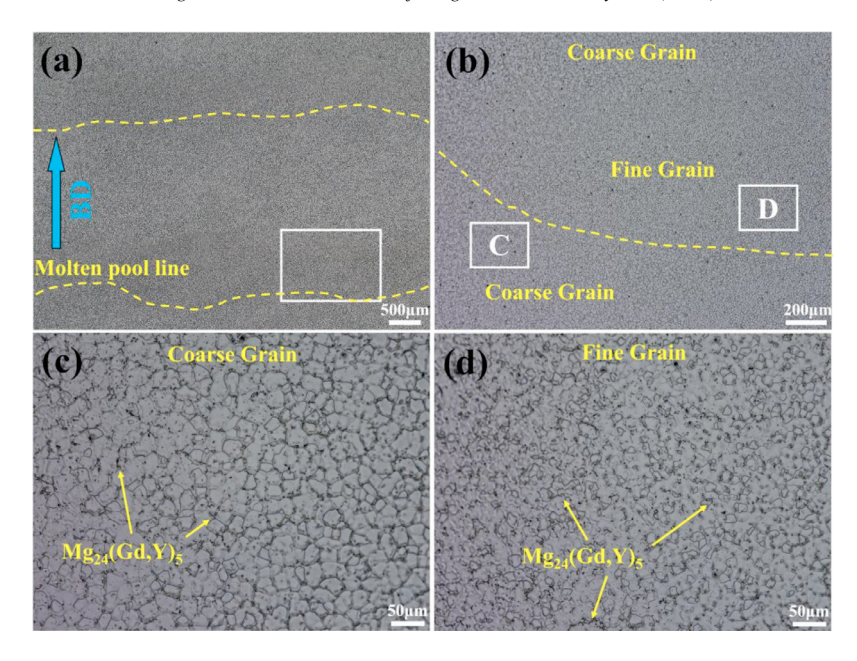


Fig. 4. (a) Macrostructure morphology, and OM images showing morphologies of (b) within the coarse grain and fine grain, (c) coarse grain and (d) fine grain.

the high diffusion rate of H atoms in magnesium (about 10^{-11} m²/s), the trace hydrogen remaining in the alloy (probably derived from the WAAM process or environmental adsorption) combines with the enriched Gd/Y to form a cubic structure of (Gd, Y) H₂ intermetallic compounds. In the sample with T6 treatment, the diffraction peak of (Gd, Y) H₂ is significantly weakened. This may be because the production of β ' precipitate phase consumes part of (Gd, Y) H₂ and affects its diffraction peak. This will be discussed in detail in "Section 3.4".

3.2. Microstructure of as-built specimen

Fig. 4 shows OM images of as-built GW63K alloys. Since the WAAM process is a layer-by-layer deposition process, a layered structure composed of fusion lines can be observed by the OM observation (Fig. 4(a)). Areas with obvious differences in grain size were produced across the molten pool line as shown in Fig. 4(b)-(d). The WAAM deposition technique induces an in-situ heat treatment effect, whereby the grains positioned below the molten pool line undergo growth as a result of higher temperatures. At the same time, the interlayer dwelling leads to a decrease in the temperature of the thin wall after the previous layer is deposited, enhancing its heterogeneous nucleation, thereby obtaining relatively fine grains above the molten pool line. At the same time, most of the grain boundaries of the WAAM-GW63K sample are obviously occupied by the Mg₂₄(Gd,Y)₅ eutectic phase, as shown by the yellow arrows. Additionally, the samples fabricated via WAAM showed no crack defects and only very few pores were detected.

The SEM and EDS images of the as-built GW63K were shown in Fig. 5. The microstructure of the as-built sample primarily consisted of fine equiaxed α -Mg grains along

with island-like Mg₂₄(Gd,Y)₅ eutectic phases. As depicted in Fig. 5(b), three distinct regions of varying brightness are observed: the darkest region corresponds to the α -Mg phase, the brightest region corresponds to the Mg₂₄(Gd,Y)₅ phases, and the gray region is a supersaturated α -Mg matrix containing RE elements. According to literature reports [33,34], the irregularly shaped phase at point A and point B is a RE-rich phase, mainly containing Mg₂₄(Gd,Y)₅, with the latter being dominant. Moreover, Fig. 5(d) reveals the presence of a cuboid-shaped phase on the α -Mg matrix, measuring approximately 500 nm in size. This phase is common in Mg-RE alloys and is typically identified as the (Gd, Y) H₂ phase [35]. Fig. $5(e_1) \sim (e_4)$ illustrate the corresponding elemental distribution of Mg, Gd, Y, and Zr, indicating that Gd and Y are enriched in the eutectic regions. The gray regions observed along the grain boundaries indicate the segregation of Gd and Y, implying that these elements are expelled to the solid-liquid interface during the solidification process of WAAM.

The EBSD analysis was carried out in the XOZ, YOZ, and XOY planes of this deposit to investigate texture characteristics and grain morphologies, as shown in Fig. 5(f). The microstructure reveals fully equiaxed ultrafine grains across all three orientations, with an average grain size of approximately 16 μm. Display the pole figures for the XOZ, YOZ, and XOY planes, respectively. The (0001), (1010), and (1120) pole figures in Fig. 5(g-i) display a characteristic homogeneous grain orientation distribution, with the highest texture intensities of 3.399, 4.025, and 4.124. This suggests a faint texture in the sample, uniformly distributed in all three directions, without any prominent crystallographic orientation in the deposit.

TEM analysis was performed to further confirm the type of rare earth-rich phase in the GW63K alloy. The bright field morphology and selected area electron diffraction (SAED)

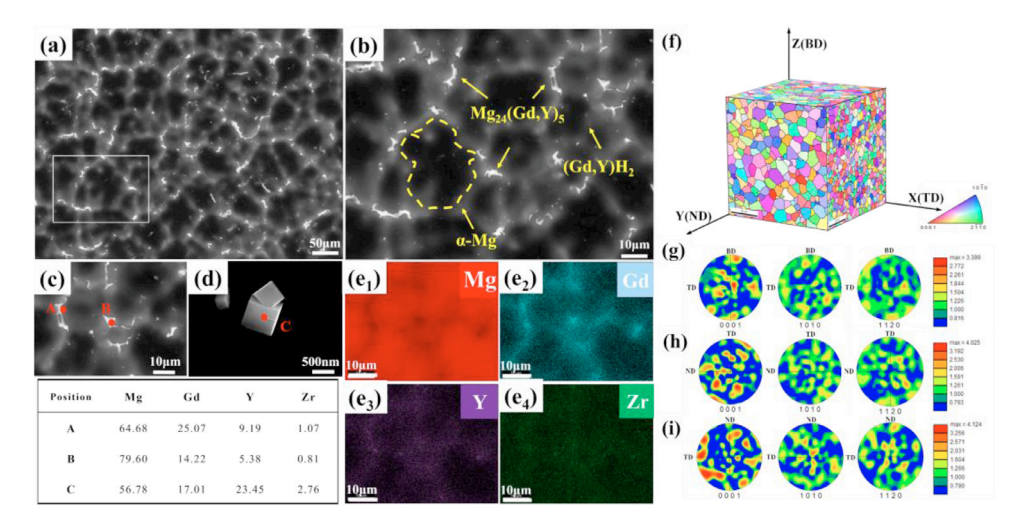


Fig. 5. (a-d) SEM images of the as-built GW63K alloy; (e_1-e_4) element distribution maps of Mg, Gd, Y, and Zr; (f) grain morphologies and (g-i) texture states of the XOZ, YOZ, and XOY planes, respectively.

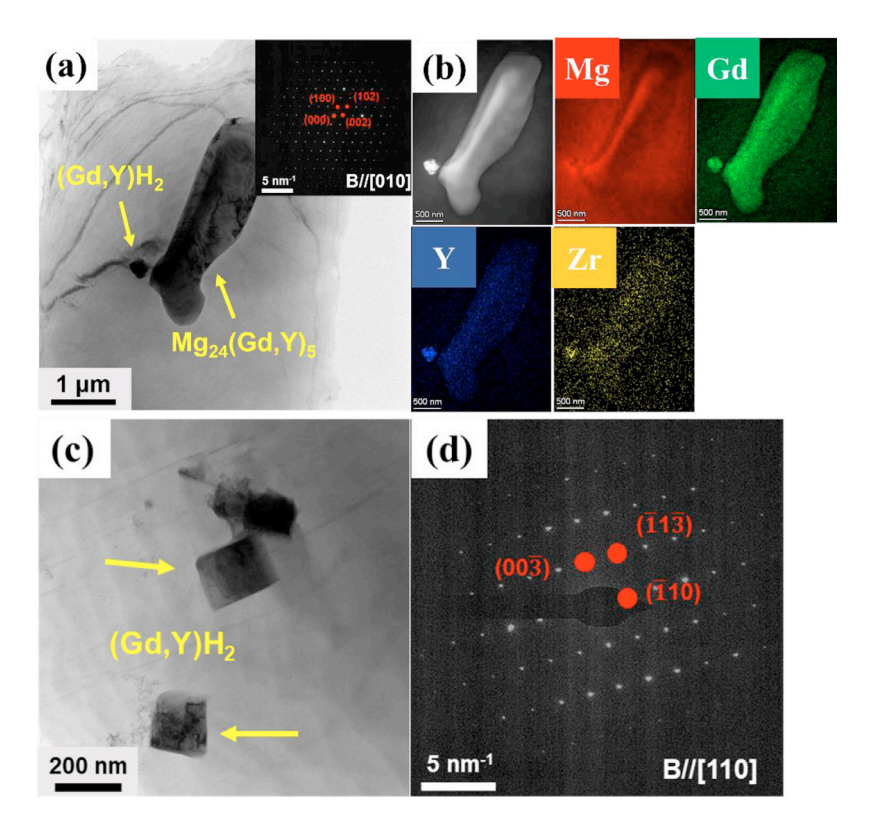


Fig. 6. (a) Bright-field image of the $Mg_{24}(Gd, Y)_5$ and the corresponding SAED pattern (B // [010]) and (b) HAADF-TEM mappings; (c) the (Gd,Y)H₂ phase and (d) the corresponding SAED pattern (B // [110]).

pattern indicate a Gd/Y rich precipitate of Mg₂₄(Gd,Y)₅ in the as-built GW63K alloy, as seen in Fig. 6(a). High-angle annular dark field scanning transmission electron microscopy (HAADF-STEM), coupled with energy dispersive X-ray (EDX) mapping, demonstrates pronounced enrichment of Gd and Y elements within the island-like secondary phase, which is primarily localized along the grain boundaries (Fig. 6b). Interestingly, a face-centered cubic (FCC) lattice structure was found in cubic particles of 200 nm or less in Fig. 6(c), with obvious enrichment of Gd and Y elements.

From the SAED pattern in Fig. 6(d) and previous literature [34,35], the cuboid particles could be confirmed as (Gd,Y)H₂. The formation of the (Gd,Y)H₂ phase takes place when rare earth elements react with hydrogen in the liquid phase, leading to the production of rare earth hydrides. The formation of (Gd,Y)H₂ will deteriorate the mechanical properties, especially EL. Thanks to the extremely low content of (Gd,Y)H₂ in our CMT-WAAM GW63K alloys, its adverse effects are not obvious.

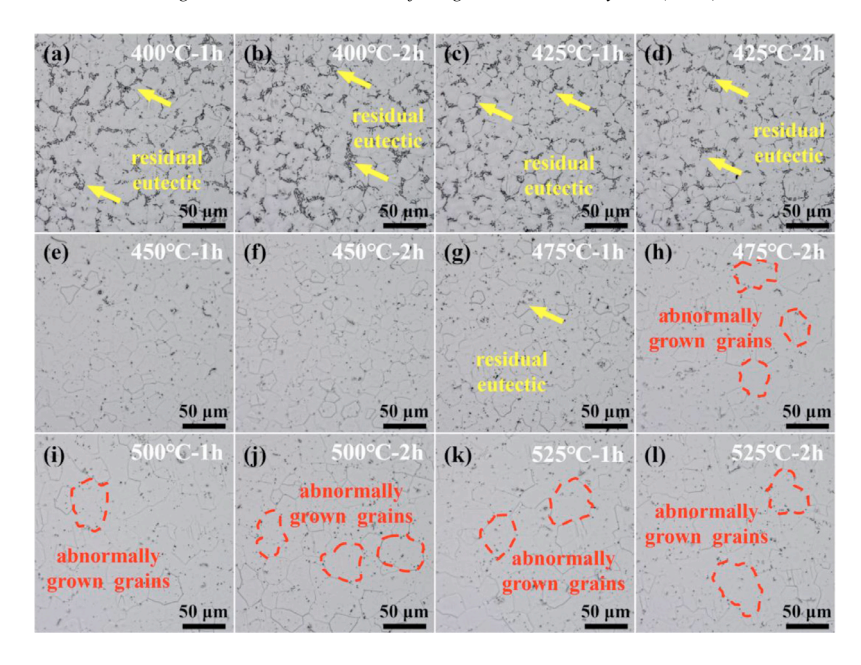


Fig. 7. Microstructure of the WAAM GW63K alloy under solution treatment at (a)-(b) 400 °C, (c)-(d) 425 °C, (e)-(f) 450 °C, (g)-(h) 475 °C, (i)-(j) 500 °C, (k)-(l) 525 °C.

3.3. Microstructure evolution of heat treatment specimen

Fig. 7 presents the OM images of the microstructure of WAAM GW63K alloy at different solution treatment temperatures and times. Figs. 7(a)-(d) reveal that after solution treatment at 400 °C and 425 °C for 1-2 h, a significant amount of residual eutectic phase remains at the grain boundaries, which fails to completely dissolve. In contrast, Figs. 7(e) and (f) show that at 450 °C for 1-2 h, the eutectic phase at the grain boundaries is completely dissolved, and submicron precipitates are uniformly dispersed within the α -Mg matrix. Figs. 7(g)-(h) demonstrate that the eutectic phase is nearly entirely dissolved after solution treatment at 475 °C for 1 h, but the grains grow abnormally after holding for 2 h. As shown in Figs. 7(i)-(l), when the solution treatment temperature exceeds 475 °C, the grains of the WAAM GW63K alloy grow abnormally (> 100 \mu m), which is harmful to the properties of the alloy. In summary, short-time solution treatment at 450 °C can optimize the grain size and precipitation morphology of WAAM GW63K alloy. In order to achieve a better solution effect, 450 °C for 2 h was chosen as the optimal T4 heat treatment condition for this study.

The age-hardening response was explored at an aging temperature of 200 °C for WAAM GW63K samples subjected to T4 treatment, as illustrated in Fig. 8. The hardness of the T4-treated sample was nearly 71 ± 1 HV_{0.1}, which is inferior to that of the as-built sample $(81 \pm 2$ HV_{0.1}). The reduction in hardness is attributed to the diffusion of Gd and Y elements, coupled with a decreased volume fraction of the high-hardness Mg₂₄(Gd, Y)₅ eutectic phase during the T4 heat treatment. Upon aging, hardness first increases over time, peaking at approximately 96 h, before progressively declining. The rapid initial increase in hardness is due to the high supersaturation of alloying elements, leading to a rapid and large

amounts of precipitates at the earlier aging state. Although the second peak appears in the figure, in general, the strengthening effect of Mg-RE alloy in the first aging stage is ideal, and the strengthening effect gradually weakens thereafter, so the hardness change of the second peak is often lower than that of the first peak. At the first peak, the distribution of the precipitated phase is more uniform and stable. Choosing the first peak as the final aging system can be more easily controlled and optimized to avoid unstable performance caused by overaging. Based on the curve fitting result, the aging condition of 200 °C for 96 h was identified as the peak aging regime, achieving a maximum hardness of 119 \pm 2 HV_{0.1}.

Fig. 9 presents the OM and SEM images of the WAAM-T4 and WAAM-T6 samples. The results show that the $Mg_{24}(Gd,Y)_5$ phase is greatly affected by T4 and T6 heat treatments of WAAM-GW63K sample. Specifically, the irregular $Mg_{24}(Gd,Y)_5$ phase near the grain boundaries largely disappear, with only a minimal amount of residual phase remaining. As shown in Fig. 9(a) and (c), there is no obvious difference in the macro-morphology between the samples treated with T4 and T6. Furthermore, Fig. 9(b) and (d) indicate that a limited number of $(Gd,Y)H_2$ phase have yet to dissolve completely into the α -Mg matrix.

Fig. 10 presents the electron backscatter diffraction (EBSD) analysis results for the WAAM-T4 and WAAM-T6 samples. Fig. 10(a₂) and (b₂) display the Kernel Average Misorientation (KAM) maps for different samples. KAM reflects the local orientation gradients, with green regions indicating areas of pronounced misorientation. It is observed that both the T4 and T6 treated samples exhibit uniform KAM values, without any discernible variation between them. Compared to the microstructure of the as-built sample, the grain size of both the WAAM-T4 (Fig. 10(a₃)) and WAAM-T6 (Fig. 10(b₃)) samples showed no significant increase, with

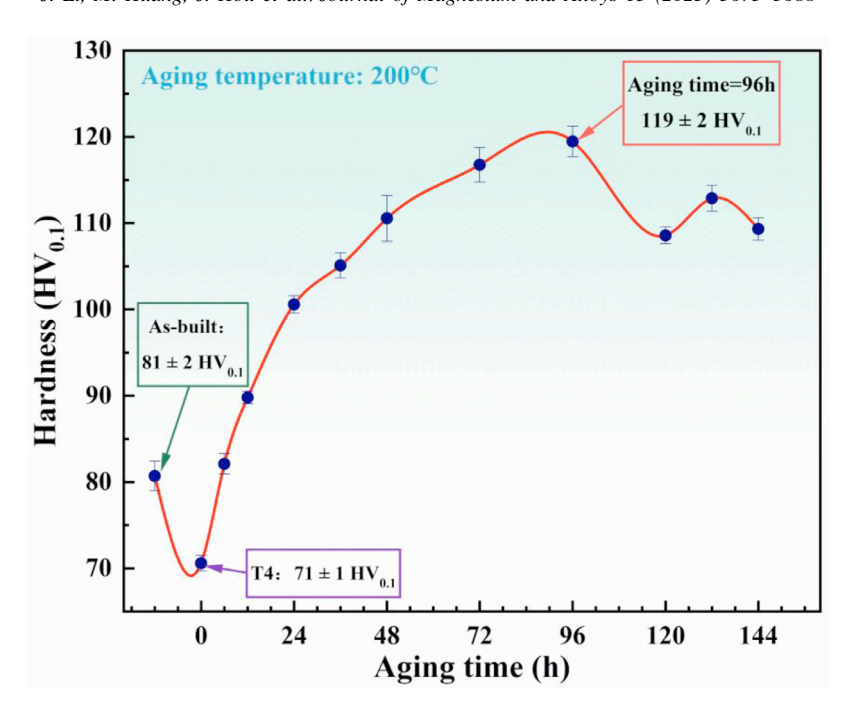


Fig. 8. Age hardening curves of T6 treatment.

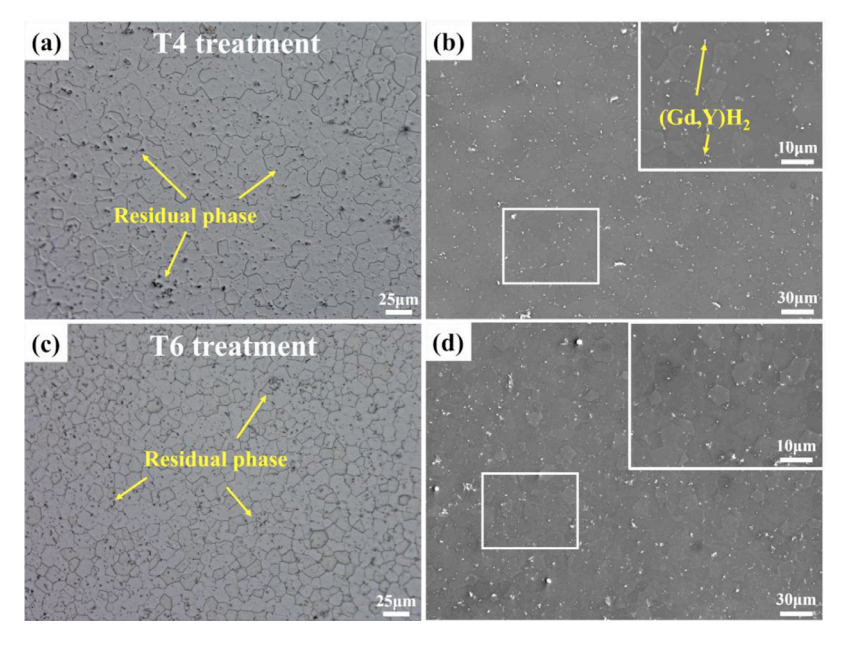


Fig. 9. (a) OM; and (b) SEM images of the T4 treated specimen; (c) OM; and (d) SEM images of the T6 treated specimen.

the average grain size remaining at approximately 18 μ m. This stability in grain size is primarily attributed to the pinning effect exerted by Zr particles and (Gd,Y)H₂ phase at the grain boundaries, which effectively impede grain growth by anchoring the boundaries [36]. Additionally, the T4 and T6 treated samples do not display any pronounced preferred orientation, maintaining a consistent equiaxed grain structure throughout [37].

Figs. 11(a) and (b) present TEM images of the WAAM-T4 sample. No precipitate phase is observed within the grains, while a small amount of residual phase remains at the grain

boundaries. The EDS analysis shown in Fig. 11(c) indicates that the residual phase at the grain boundaries is enriched with Gd and Y elements, and its morphology and elemental distribution are consistent with the (Gd,Y)H₂ phase described in Fig. 6(c). In previous studies [35], it was shown that the (Gd,Y)H₂ phase usually has stronger high temperature resistance. These phases are primarily attributed to the residual (Gd,Y)H₂ phase present in the as-built sample, which remains after a brief high-temperature solution treatment. This phase plays a crucial role in impeding grain growth and maintaining a fine-grained structure post-heat treatment.

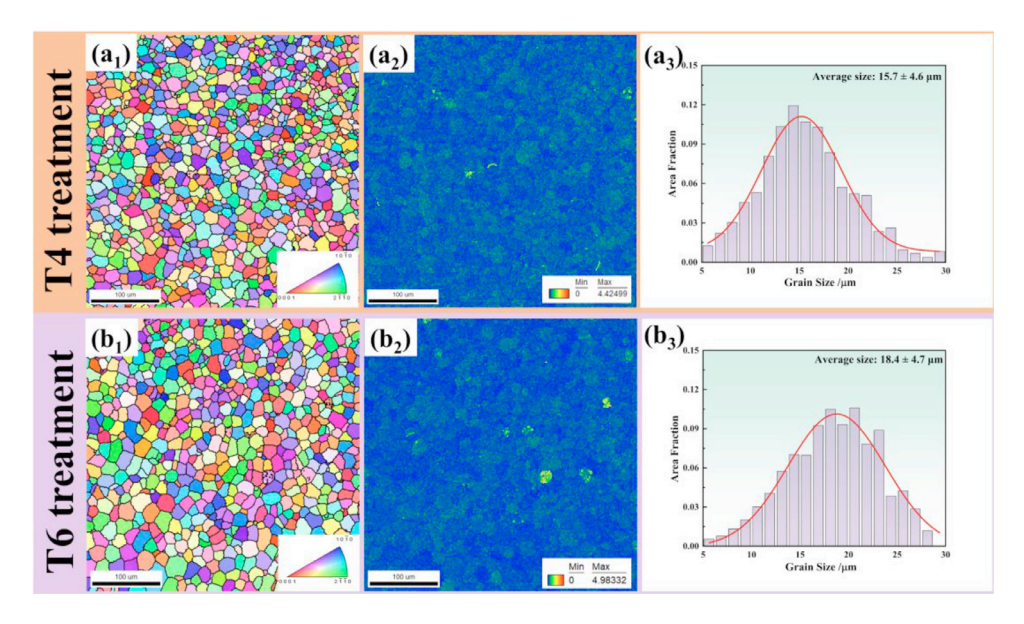


Fig. 10. IPF, KAM, and grain size distribution of the WAAM-GW63K samples with the (a₁-a₃) T4 and (b₁-b₃) T6 treatment.

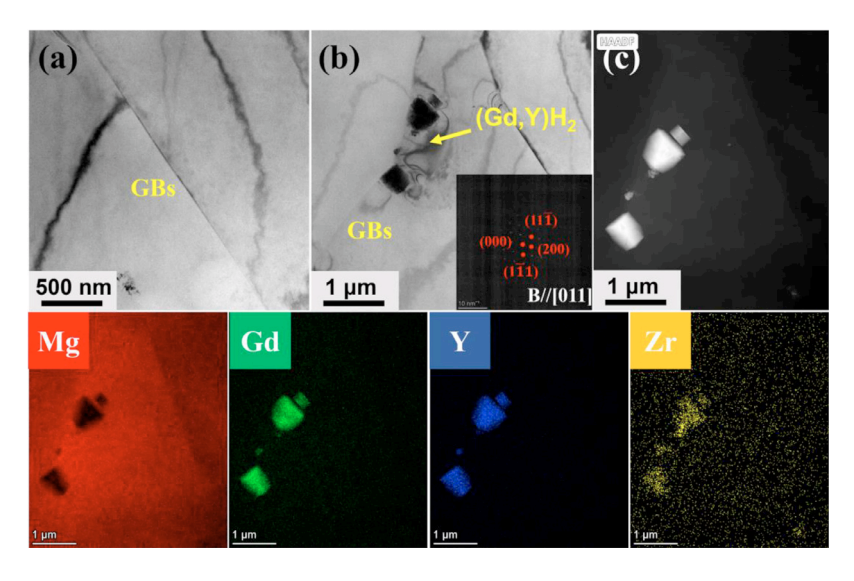


Fig. 11. TEM results of the WAAM GW63K alloy under the T4 condition (450 °C × 2 h): (a) (b) inner grain and around grain boundary; (c) the HAADF and EDS mapping images of grain-boundary phases.

According to the above-mentioned results, it is inferred that no obvious difference occurred on both grain size and precipitates distribution from T4 to T6 heat treatment. Nanoscale precipitates, however, are typically formed following theT6 treatment in Mg-Gd-Y-Zr alloys. To detect and characterize these fine precipitates, TEM analysis is conducted for detailed insights into the morphology and distribution at the nano-scale. In Fig. 12(a), the morphology and distribution of the β' phase are presented. The β' phase in the T6 treatment sample is arranged in an elliptical triangular formation along the matrix. The EDX mapping results shown in Fig. 12(b) indicate that the nano β' precipitate phase is predominantly enriched with Gd and Y. The SAED pattern in Fig. 12(c) shows that there are additional diffraction spots at the diffraction spots of the substrate. When cross-referenced with the characteristics of the precipitated phase in Mg-RE alloy reported

by previous researchers [35], these findings confirm the presence of the β' phase. The orientation relationship between the nano β' phase and the matrix are defined as (001) β' // (0001) $_{\alpha}$ and [100] β' // [1 $\bar{2}$ 10] $_{\alpha}$. As shown in Fig. 12(e), the nano β' phase has dimensions of approximately 32.9 nm in length and 10.5 nm in width.

3.4. Tensile properties and fracture morphology analysis

The mechanical performance was tested and compared between the as-built and T4 and T6 heat treated WAAM samples. Fig. 13 illustrates the engineering tensile stress-strain curves and tensile properties of samples evaluated in both the traveling direction (TD) and the building direction (BD), specifying the ultimate tensile strength (UTS), yield strength (YS), and elongation (EL). The as-built sample along the

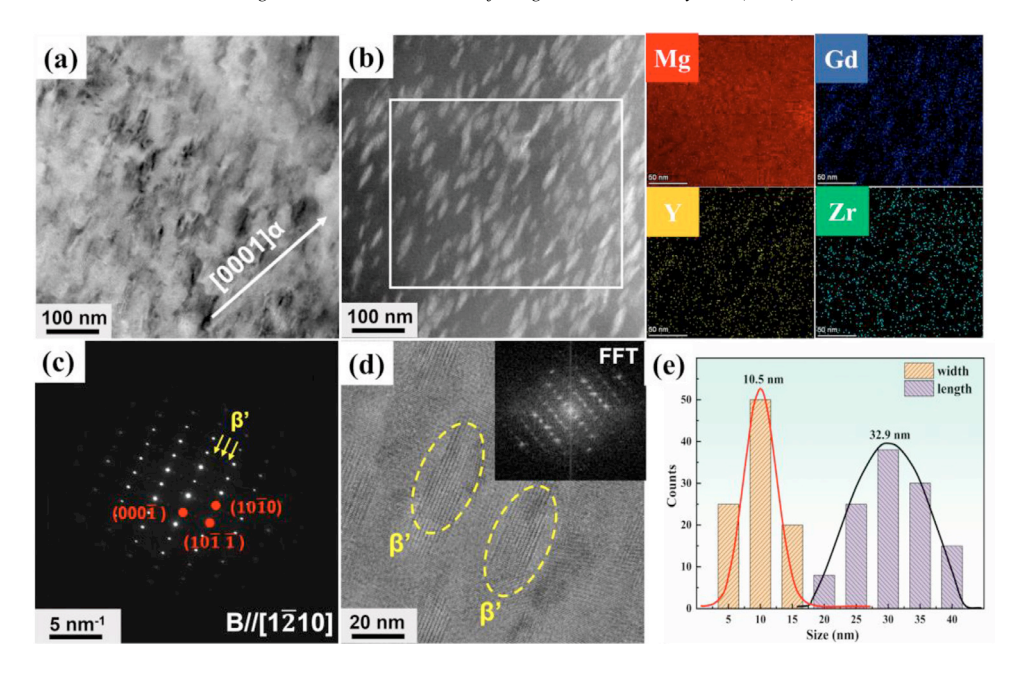


Fig. 12. TEM results of the WAAM-GW63K under T6 treatment: (a) TEM image and (b) HAADF image and EDS results of Mg, Gd, Y, Zr; (c) SAED pattern of the matrix (along the $[1\bar{2}10]_{\alpha}$ zone axis); (d) HR-TEM image and FFT of the nano-precipitates and (e) the size distribution of the nano-precipitates.

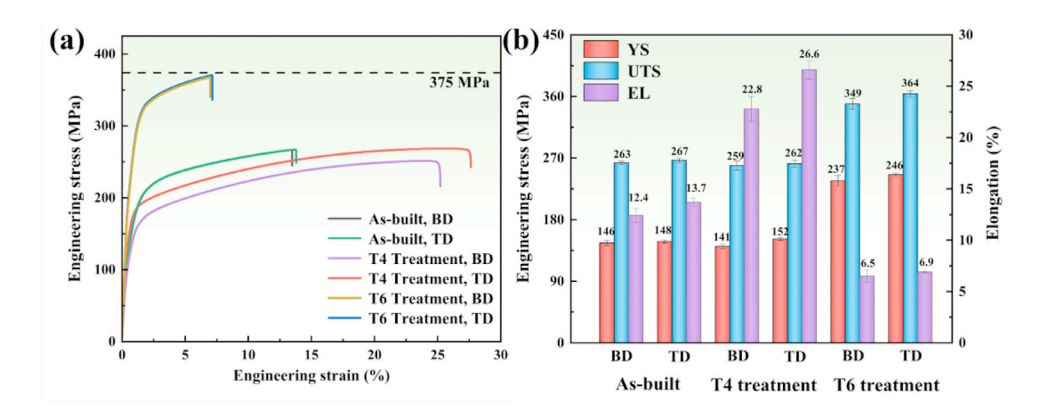


Fig. 13. Tensile properties of as-built, T4 and T6 specimens: (a) stress-strain curves; (b) statistics of tensile properties.

TD demonstrates a yield strength of 148 \pm 1 MPa, an ultimate tensile strength of 267 ± 3 MPa, and an elongation of 13.7 \pm 0.1%. After the solution treatment, the UTS and YS of the T4 sample in the TD show a slight decrease, while the EL improves markedly, reaching 26.6 \pm 0.9%. The main reason for the improvement of EL is that the solid solution strengthening effect after the introduction of rare earth elements hinders the dislocation movement through lattice distortion, thereby enhancing the material's ability to resist deformation. At the same time, the stabilization effect at the grain boundary improves the toughness of the alloy and reduces the risk of brittle fracture. The aging procedure markedly improves the strength of the T6 sample. More specifically, the YS of the T6 sample along the TD is 246 \pm 2 MPa, the UTS MPa, and the EL is $6.9 \pm 0.2\%$, which are 52% and 36% higher than those of the as-built sample, respectively. Also, the tensile qualities at room temperature along the BD follow the same scheme, so they won't be talked about again here. The isotropic strength is due to the equiaxed grain structure. The results are also compared with previously reported Mg alloys produced using WAAM technology, as listed in Table 3.

Table 3 provides the tensile properties of the WAAM-processed magnesium alloys developed in our study, along with those reported in previous literature. Fig. 14 presents a summary chart comparing the yield strength (YS) and elongation (EL) values, as specified in Table 3. It is demonstrating that the performance of the WAAM GW63K alloy in both As-built, T4 and T6 conditions in this work surpasses that of other Mg-Gd-Y and AZ series alloys reported to date, establishing it as a formidable contender for lightweight, load-bearing components in numerous essential engineering applications.

Fig. 15 presents SEM fracture images of tensile specimens, illustrating the failure modes of the as-built, T4-treatment, and T6-treatment specimens. As shown in Fig. 15(a-b), the as-

Table 3
Mg alloys processed with WAAM obtained in this study and reported in previous works.

Materials Composition (wt.%)	States	Tensile properties		Ref.		
		UTS (MPa)	YS (MPa)	EL (%)	-	
GW63K Mg-6.4Gd-3.2Y-0.4Zr	As-built	267	148	13.7	This work	
	WAAM-T4	262	152	26.6		
	WAAM-T6	364	246	6.9		
GW63K Mg-6Gd-3Y-0.5Zr	As-built	232	150	8.2	[35]	
	WAAM-T6	345	218	5.2		
GW63K Mg-5.9Gd-2.8Y-0.7Zr	Mg-5.9Gd-2.8Y-0.7Zr	As-built	263	162	13.2	[34]
	WAAM-T4	257	153	17.9		
	WAAM-T5	350	227	5.5		
	WAAM-T6	320	199	6.7		
GW63K	Mg-6Gd-3Y-0.5Zr	As-built	230	161	11.0	[33]
	WAAM-T4	255	150	22.0		
		WAAM-T6	338	230	3.6	
GWZ431K	Mg-4.4Gd-2.2Y-1.0Zn-0.5Zr	As-built	224	123	12.7	[31]
·	WAAM-T4	234	117	17.7		
	WAAM-T6	288	157	17.1		
GWZ831K	Mg-8.1Gd-2.6Y-0.7Zn-0.5Zr	As-built	242	163	7.0	[38]
GWZ941K	Mg-8Gd-4Y-1Zn-0.5Zr	As-built	243	167	5.2	[39]
		WAAM-T4	220	132	5.9	
	WAAM-T6	258	231	1.1		
GWZ1031K Mg-10Gd-3Y-1Zn-0.5Zr	As-built	271	154	8.7	[32]	
	WAAM-T4	287	170	16.5		
	WAAM-T6	337	214	2.8		
WE43	Mg-4Y-2Nd-1Gd-0.5Zr	As-built	271	199	8.1	[30]
WE43	Mg-3.7Y-2.1Nd-1.2Gd-0.3Zr	As-built	226	149	6.8	[40]
GW92 Mg-9.54Gd-1.82Y-0.44Zr	As-built	253	146	8.7	[37]	
	WAAM-T6	360	235	10.8		
GW93K	Mg-9Gd-3Y-0.5Zr	WAAM-T6	392	262	3.3	[41]
AZ31	Mg-3.12Al-0.84Zn-0.2Mn	As-built	210	131	10.5	[42]
AZ61	Mg-6.02Al-0.88Zn-0.15Mn	As-built	260	105	16	[43]
AZ80M	Mg-8.5Al-0.45Zn-0.03Mn-0.15Ca-0.2Y	As-built	308	146	15	[27]
AZ91D	Mg-8.99Al-0.65Zn-0.26Mn	As-built	244	111	11.7	[44]

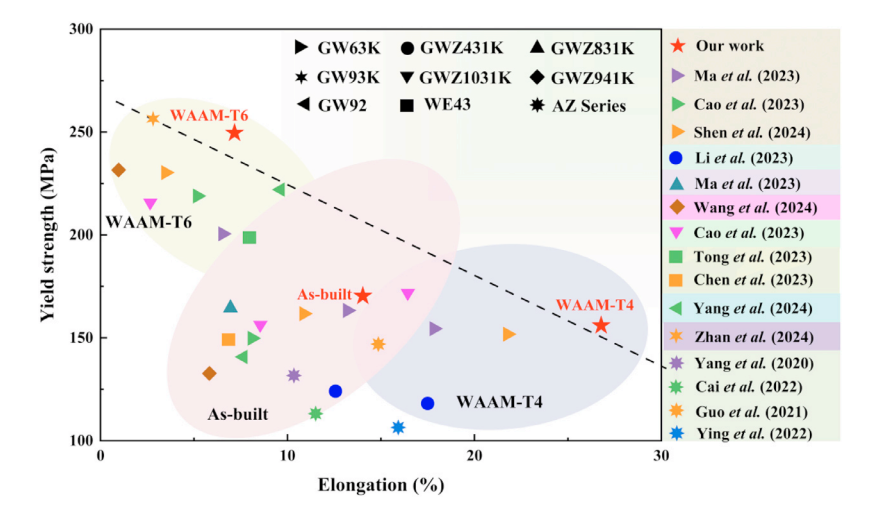


Fig. 14. YS versus EL of the Mg alloy fabricated by WAAM in our work and in published papers.

built specimen exhibits a small number of dimples along with numerous secondary cracks, indicative of a typical ductile-brittle mixed fracture mode. Fig. 15(a) reveals the presence of cracks within the coarse eutectic phase in the fracture microstructure of the as-built GW63K alloy, including secondary cracks within the dimples (Fig. 15(b)), which also

originate from the fracture of the coarse eutectic phase. These fractured eutectic phases contribute to the moderate ductility of the as-built sample, leading to early failure. In contrast, the WAAM-T4 specimen displays numerous deep dimples and ductile tear ridges (Fig. 15(c-d)), suggesting a predominantly ductile fracture mode. The WAAM-T6 sample, how-

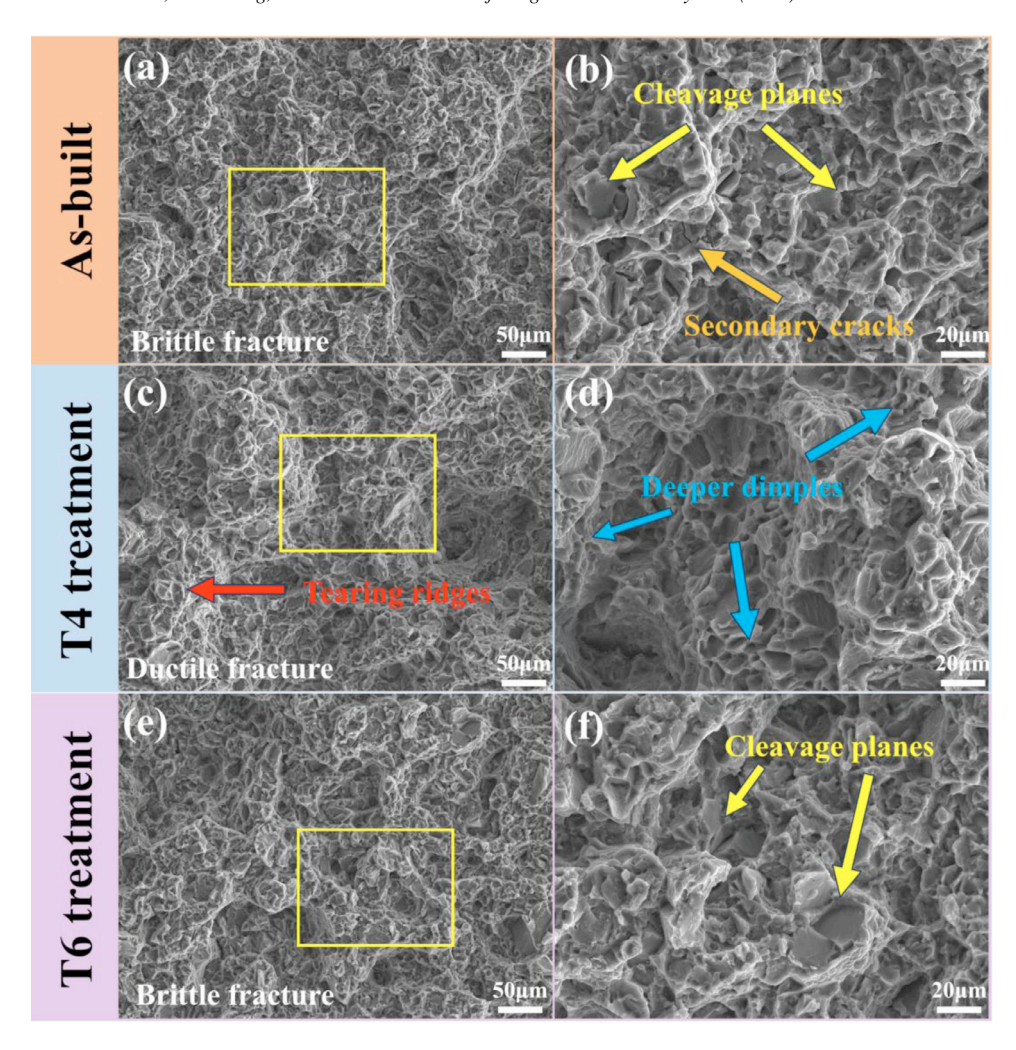


Fig. 15. SEM fractographies of (a, b) as-built, (c, d) T4 treatment and (e, f) T6 treatment specimens.

ever, exhibits a ductile-brittle mixed fracture mode, with the appearance of coarse cleavage planes in the fracture surface (Fig. 15(f)). This is attributed to the elevated density of nano β' precipitates generated during the aging process, which confer substantial precipitation strengthening. These finely sized nanoprecipitates are more resistant to shearing and effectively impede the motion of basal dislocations, thereby promoting the formation of additional slip planes [33] .

4. Discussions

4.1. Microstructure evolution

This study revealed that the microstructure of metal WAAM samples is inheritable, with the microstructure and other properties of the raw material being retained in the layer by layer melting and solidification sample during the additive manufacturing process [45]. Fig. 16 depicts a schematic representation of the microstructural evolution occurring during the preparation and thermal treatment of WAAM-GW63K. Under the heating of the arc, the wire melts and forms molten droplets, driven by surface tension. These droplets are de-

posited into the molten pool as the wire advances, where rapid solidification occurs to form the deposition layer. The high-energy density arc in the WAAM process produces a molten pool for the Mg-based alloy, promoting the refining of Zr particles and increasing the solute concentration of Zr [46]. Zr particles act as effective heterogeneous nucleation sites within the α -Mg matrix, facilitating grain refinement and the formation of equiaxed crystals [47]. During solidification, micro segregation causes Gd and Y elements to concentrate along the grain boundaries, resulting in the formation of eutectic phases. This unique solidification process corresponds to step 1 through step 3 as shown in Fig. 16.

The (Gd,Y)H₂ phase in the WAAM-GW63K alloy forms through the rapid solidification of RE element particles that are enriched in the GW63K wire after arc heating and melting. This phase is minuscule, measuring roughly 300 nm. The brief, high-temperature solution treatment at 450 °C for 2 h facilitated the swift and complete dissolution of the Mg₂₄(Gd,Y)₅ phase, while the Zr particles exerted a pinning action on the grain boundaries, preventing grain coarsening. After the T4 treatment, the microstructure of the GW63K alloy shows that the majority of the Mg₂₄(Gd,Y)₅ phase has

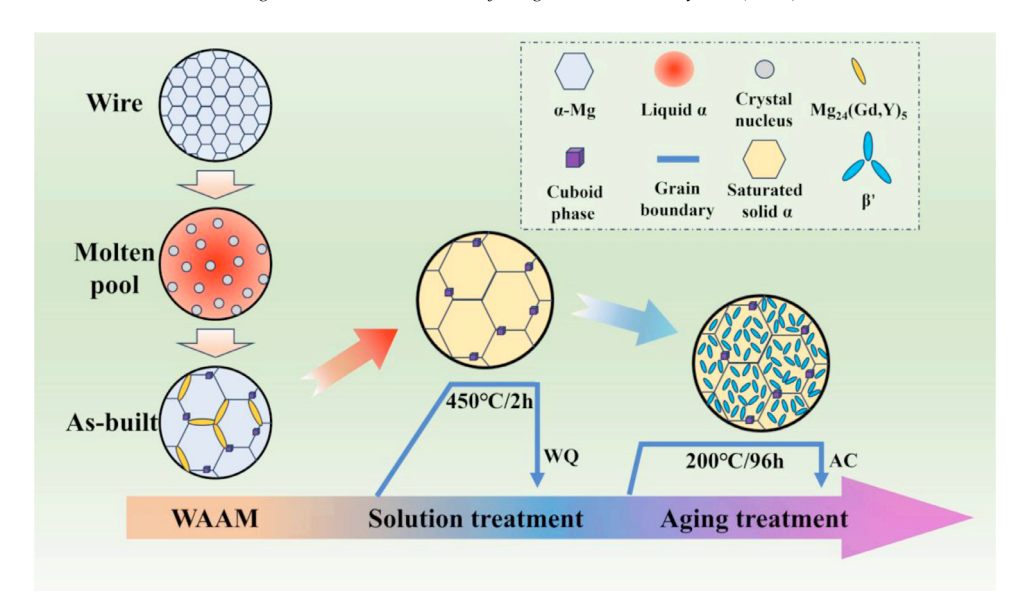


Fig. 16. Schematic illustrate for the microstructure evolution of the WAAM GW63K alloy during heat treatment.

dissolved into the α -Mg matrix, creating a supersaturated α -Mg phase enriched with Gd and Y atoms, corresponding to step 5 mentioned above.

According to the age hardening curve, the peak aging time of the WAAM-GW63K alloy at 200 °C is 96 h, which consists of a small number of irregular $Mg_{24}(Gd, Y)_5$ particles and a high density of uniformly distributed nano-sized β' precipitates within the α -Mg matrix. The precipitation sequence of the Mg-Gd-Y-Zr alloy, as established by Zheng et al. [48], follows: SSSS (super-saturated solid solution) \rightarrow clusters \rightarrow nucleation of β' (major) / β_H (minor) \rightarrow precipitation of β' (major) / β_M , β'_T (minor) \rightarrow β_1 \rightarrow β (equilibrium). Under peak aging conditions, the strengthening structure is primarily defect-free β' precipitates, with minimal interaction among them. As the aging time increases in the Mg-Gd-Y-Zr alloy, β' precipitates gradually form from the supersaturated matrix, functioning as the principal reinforcement phase and significantly enhancing the magnesium alloy's overall strength.

4.2. Strengthening mechanism

The strength contribution values of the GW63K alloy under different states are shown in Fig. 17. In general, the increase in yield strengthening (σ_y) of the Mg-Gd-Y-Zr alloys is represented as follows:

$$\sigma_{y} = \sigma_{0} + \sigma_{gb} + \sigma_{GND} + \sigma_{P} + \sigma_{SS} + \sigma_{\beta'} \tag{1}$$

where σ_0 is the base yield strength of the matrix, σ_{gb} accounts for the grain boundary strengthening, σ_{SS} represents the solid solution strengthening, σ_P corresponds to the second phase strengthening, $\sigma_{\beta'}$ is the precipitation strengthening, and σ_{GND} accounts for the dislocation strengthening. Where σ_0 is the strength of pure Mg with a value of 23 MPa [49].

It is a commonly held belief that fine grains are superior to coarse grains in terms of their performance in strengthening materials [50]. Based on the Hall-Petch relationship [30], we

calculated the grain boundary strengthening contribution in the as-built GW63K alloy:

$$\Delta \sigma_{gb} = k \cdot d^{-\frac{1}{2}} \tag{2}$$

where d is the average grain size, and k is the H-P slope. This relationship estimates the enhancement in yield strength resulting from grain refining. Considering other magnesium alloys and their k values [51], in Mg-Gd-Y series alloys, k=303 MPa/ μ m^{1/2} [49]. This investigation reveals that fine equiaxed grains predominate the microstructure (Fig. 4(f)), with an average grain size of roughly 15.7 μ m. Consequently, 76.5 MPa signifies the impact of grain boundary strengthening on the YS. According to Fig. 10, since aging treatment does not lead to grain growth, $\sigma_{gb}(T4)$ and $\sigma_{gb}(T6)$ are both 70.6 MPa.

Geometrically necessary dislocation (GND) also plays a role in YS. The approximate GND density can be determined by calculating the average misorientation between neighboring EBSD data locations. The KAM diagram illustrates the distribution and extent of GNDs within the microstructure [52]. Consequently, the GND density can be calculated from the KAM diagram at various material states [53]. According to He et al. [54], the GND density σ^{GND} is related to the misorientation angle θ :

$$\rho^{GND} = 2\theta/\mu b \tag{3}$$

here, θ represents the local misorientation, μ is the unit length of the point (with $\mu=1~\mu m$, equivalent to the scanning step length), and b is the Burgers vector (b=0.32~nm). The calculated μ values are 0.34° for the T4 condition and 0.42° for the as-built condition. Based on Eq. (3), the mean GND densities are $3.71\times10^{13}~m^{-2}$ for the T4 condition and $4.58\times10^{13}~m^{-2}$ for the as-built condition. A further way to evaluate residual dislocation hardening is by the following method [55]:

$$\sigma_{GND} = M\alpha Gb\sqrt{\rho^{GND}} \tag{4}$$

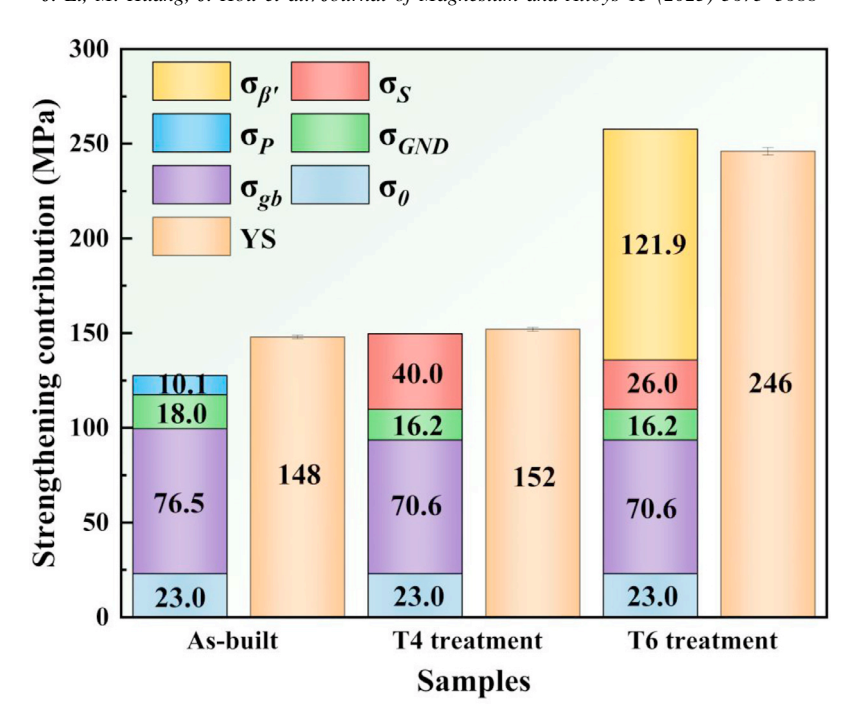


Fig. 17. Strengthening contributions of YS for the WAAM GW63K alloy.

where an M Taylor factor value of ~ 2.5 is used for simplicity; α is a constant (= 0.2) [56] and G is the shear modulus (\approx 16,600 MPa). The computed dislocation strengthening values indicate that the as-built value is 18.0 MPa, while the treated value is 16.2 MPa (T4 & T6 treatment).

The second phase can enhance the YS of WAAM GW63K alloy. These second phase particles are distributed along the grain boundaries, where they serve to reinforce the load transfer from the α -Mg matrix. According to the research of Li et al. [34], the contribution of the second phase to YS can be determined as follows:

$$\sigma_P = \frac{1}{2} f_p \sigma_y \tag{5}$$

where σ_P and σ_y are the volume fraction of the second phase and the YS of the as-built GW63K alloy (148 MPa). Based on the SEM images, the f_p was approximately 13.6% of the asbuilt GW63K alloy, resulting in a strengthening contribution of ~ 10.1 MPa from the second phase.

It is usually the T4 treatment that dissolves the eutectic phases into the matrix of Mg-RE alloys. By causing lattice distortion, the strength can be improved by preventing dislocation movement, as shown in the following equation [1]:

$$\sigma_{SS} = \sum k_i c_i^n \tag{6}$$

In this context, the constant n is considered to be 1/2 for the ternary solid solution strengthening in Mg-Gd-Y alloys. The term k_i represents the factor associated with solute i, while c_i denotes the solid solubility of solute i within the matrix [57]. The k_i factors for the individual solute components were taken as 683 MPa(at.%) $^{-1/2}$ for the Gd element and 737 MPa(at.%) $^{-1/2}$ for the Y elements [1]. Post-solution heat

treatment, Gd and Y were effectively incorporated into the α -Mg matrix, as demonstrated by EDS measurements indicating compositions of 1.33 at.% Gd and 1.05 at.% Y. Therefore, the value of $\sigma_{SS}(T4)$ was determined to be 40.0 MPa. As a result of ageing heat treatment, the value of was determined to be 26.0 MPa.

Mg-Gd-Y alloys are well recognized for their β precipitation series [58–60]. The role of intragranular precipitates in the precipitation strengthening of Mg-Gd-Y alloys is significant. Nano-sized β' precipitates are uniformly and discretely distributed inside the supersaturated α -Mg solid solution, significantly contributing to the enhancement of the alloy's strength [61]. In this experiment, the β' precipitates had a projected length of approximately 32.9 nm and a width of around 10.5 nm. To simplify matters, the nano-precipitates enhance strengthening by means of the Orowan process, and their impact on YS is determined by calculating the Orowan equation [62]:

$$\sigma_{\beta'(Orowan)} = \frac{Gb}{2\pi\sqrt{1-\nu}(0.825\sqrt{\frac{d_t t_t}{f}} - 0.393d_t - 0.866t_t)} \ln\frac{0.866\sqrt{d_t t_t}}{h}$$
(7)

where G, v, b, d_t , t_t , and f are the shear modulus, Poisson's ratio, magnitude of the Burgers vector, average diameter of prismatic plates, planar thickness of prismatic plates and volume fraction of β' precipitates. The values of 0.29 was used for v [63] and the d_t and t_t of β' precipitates in the GW63K alloy was estimated at 32.9 and 10.5 nm. Accurately estimating the volume fraction of β' precipitates present considerable difficulty. As a result, the quantity of β' precipitates

were approximately assessed using TEM images, yielding an estimated value of \sim 15.0%. Therefore, the $\sigma_{\beta'(Orowan)}$ was calculated as 121.9 MPa.

In summary, grain boundary strengthening (~76.5 MPa) contributes significantly to the YS of WAAM-GW63K alloy, among which precipitation strengthening after T6 treatment (~121.9 MPa) contributes the most to YS. Although the strength has been greatly improved compared with traditionally manufactured Mg-RE alloys, its plasticity problem requires more researchers to conduct systematic research in the future in order to expand the application field of Mg-RE alloys prepared by WAAM.

5. Conclusion

In this study, the CMT-WAAM process was used to successfully prepare a single-pass multilayer of GW63K alloy thin-wall, and a high forming quality was obtained. The microstructure evolution and mechanical properties were comprehensively investigated, with both short-term high-temperature solid solution treatment and peak aging treatment employed to examine the dissolution behavior of the eutectic phase and the precipitation kinetics of the nano-precipitate phase. This guide effectively elucidates the correlation between the microstructure and properties of Mg-Gd-Y series alloys produced via WAAM. The following conclusions can be drawn:

- (1) The WAAM-GW63K alloy exhibits excellent macro and micro forming quality, with no observable macro defects. Its microstructure is composed of fine equiaxed α -Mg grains (\sim 16 μ m), along with the Mg₂₄(Gd,Y)₅ phase and a cuboid phase.
- (2) It demonstrates unprecedented isotropic mechanical properties in both building and traveling directions, attributed to the uniform, fine equiaxed grain structure that effectively mitigates component segregation and macro defects. The YS, UTS, and EL of the final sample are 148 ± 1 MPa, 267 ± 3 MPa, and $13.7 \pm 0.1\%$, respectively.
- (3) A short-time high-temperature solution treatment at 450 °C for 2 h effectively retains the original fine grains (\sim 18 μ m) while nearly completely dissolving the eutectic phase, leading to a significant enhancement in elongation (26.6 \pm 0.9%) with a slight reduction in strength.
- (4) After T6 treatment at 200 °C for 96 h, the WAAM-GW63K alloy maintains its refined grain structure while exhibiting a high density of nanoscale β' phase, leading to an outstanding strength-ductility synergy. The YS of the T6-treatment sample reaches 246 \pm 2 MPa, the UTS is 364 \pm 5 MPa, and the EL is 6.9 \pm 0.2%. In comparison to the as-built alloy, the YS and UTS of the WAAM-T6 sample demonstrate improvements of 66% and 36%, respectively.

Declaration of competing interest

The authors declare that they have no known competing financial interests or personal relationships that could have appeared to influence the work reported in this paper.

CRediT authorship contribution statement

Jiamin Li: Writing – review & editing, Formal analysis, Data curation. Meng Huang: Writing – original draft, Formal analysis. Juan Hou: Writing – review & editing, Supervision, Conceptualization. Xingbin Wang: Formal analysis, Data curation. Gaopeng Xu: Writing – review & editing, Data curation. Yi Yang: Writing – review & editing, Investigation. Ning Mo: Writing – review & editing, Formal analysis, Conceptualization. Yun Shi: Supervision, Project administration. Laichang Zhang: Writing – review & editing, Formal analysis. Weineng Tang: Resources, Conceptualization.

Acknowledgments

Supported by the Industrial Collaborative Innovation Project of Shanghai (Grant No XTCX-KJ-2022–2–11) and the National Natural Science Foundation of China (Grant No 52073176).

References

- [1] L. Gao, R.S. Chen, E.H. Han, J. Alloys Compd. 481 (2009) 379–384, doi:10.1016/j.jallcom.2009.02.131.
- [2] P.J. Apps, H. Karimzadeh, J.F. King, G.W. Lorimer, Scr. Mater. 48 (2003) 1023–1028, doi:10.1016/S1359-6462(02)00596-1.
- [3] G. Wu, C. Wang, M. Sun, W. Ding, J. Magnes. Alloys 9 (2021) 1–20, doi:10.1016/j.jma.2020.06.021.
- [4] S. Gangireddy, B. Gwalani, K. Liu, E.J. Faierson, R.S. Mishra, Addit. Manufact. 26 (2019) 53–64, doi:10.1016/j.addma.2018.12.015.
- [5] W. Rong, Y. Wu, Y. Zhang, M. Sun, J. Chen, L. Peng, et al., Mater. Charact. 126 (2017) 1–9, doi:10.1016/j.matchar.2017.02.010.
- [6] X. Xue, Y. Wu, N. Su, X. Heng, Q. Deng, Z. Chang, et al., Mater. Charact. 170 (2020) 110701, doi:10.1016/j.matchar.2020.110701.
- [7] J. Li, M. Huang, J. Fan, Y. Chen, Y. Yang, N. Mo, et al., JOM (2024), doi:10.1007/s11837-024-06889-5.
- [8] J. Zhang, S. Liu, R. Wu, L. Hou, M. Zhang, J. Magnes. Alloys 6 (2018) 277–291, doi:10.1016/j.jma.2018.08.001.
- [9] C. Zheng, S. Chen, M. Cheng, S. Zhang, Y. Li, Y. Yang, J. Magnes. Alloys 11 (2023) 4218–4234, doi:10.1016/j.jma.2023.01.006.
- [10] J. Ning, J. Zhou, B. Gao, C. Zhang, H. Shi, L. Chen, et al., J. Magnes. Alloys 12 (2024) 4140–4156, doi:10.1016/j.jma.2023.09.020.
- [11] Y. Guo, J. Li, J. Li, Z. Yang, J. Zhao, F. Xia, et al., J. Alloys Compd. 450 (2008) 446–451, doi:10.1016/j.jallcom.2006.10.125.
- [12] D. Wang, P. Fu, L. Peng, Y. Wang, W. Ding, Mater. Charact. 153 (2019) 157–168, doi:10.1016/j.matchar.2019.04.036.
- [13] J.J. Bhattacharyya, F. Wang, N. Stanford, S.R. Agnew, Acta. Mater. 146 (2018) 55–62, doi:10.1016/j.actamat.2017.12.043.
- [14] T. Honma, T. Ohkubo, K. Hono, S. Kamado, Mater. Sci. Engineer.: A 395 (2005) 301–306, doi:10.1016/j.msea.2004.12.035.
- [15] L. Chai, J. Xia, Y. Zhi, K. Chen, T. Wang, B. Song, et al., Mater. Chem. Phys. 213 (2018) 414–421, doi:10.1016/j.matchemphys.2018.04.044.
- [16] Q. Yang, S. Lv, K. Guan, Z. Xie, X. Qiu, J. Magnes. Alloys 12 (2024) 4561–4573, doi:10.1016/j.jma.2023.09.024.

- [17] B.L. Xiao, Q. Yang, J. Yang, W.G. Wang, G.M. Xie, Z.Y. Ma, J. Alloys Compd. 509 (2011) 2879–2884, doi:10.1016/j.jallcom.2010.11.147.
- [18] S. Li, D. Li, X. Zeng, W. Ding, Transac. Nonferr. Metals Soc. China 24 (2014) 3769–3776, doi:10.1016/S1003-6326(14)63531-7.
- [19] Q. Deng, Y. Wu, Y. Luo, N. Su, X. Xue, Z. Chang, et al., Mater. Charact. 165 (2020) 110377, doi:10.1016/j.matchar.2020.110377.
- [20] M. Meng, H. Zhang, Z. Gao, G. Lei, J. Yu, J. Magnes. Alloys 11 (2023) 4628–4643, doi:10.1016/j.jma.2022.02.012.
- [21] X. Zhao, Z. Yang, J. Zhang, M. Liang, L. Wang, J. Magnes. Alloys 12 (2024) 673–686, doi:10.1016/j.jma.2023.04.011.
- [22] J. Li, Q. Han, X. Han, X. Yi, J. Magnes. Alloys 12 (2024) 4709–4721, doi:10.1016/j.jma.2023.12.013.
- [23] Z. Zeng, M. Salehi, A. Kopp, S. Xu, M. Esmaily, N. Birbilis, J. Magnes. Alloys 10 (2022) 1511–1541, doi:10.1016/j.jma.2022.03.001.
- [24] C. Zhang, Z. Li, J. Zhang, H. Tang, H. Wang, J. Magnes. Alloys 11 (2023) 425–461, doi:10.1016/j.jma.2023.02.005.
- [25] K. V, N.K. B, S.K. S, V. M, Addit Manufact 55 (2022) 102802, doi:10. 1016/j.addma.2022.102802.
- [26] H. Hyer, L. Zhou, G. Benson, B. McWilliams, K. Cho, Y. Sohn, Addit. Manufact. 33 (2020) 101123, doi:10.1016/j.addma.2020.101123.
- [27] Y. Guo, G. Quan, Y. Jiang, L. Ren, L. Fan, H. Pan, J. Magnes. Alloys 9 (2021) 192–201, doi:10.1016/j.jma.2020.01.003.
- [28] X. Li, M. Zhang, X. Fang, Z. Li, G. Jiao, K. Huang, Virtual Phys. Prototyp. 18 (2023) e2170252, doi:10.1080/17452759.2023.2170252.
- [29] H. Takagi, H. Sasahara, T. Abe, H. Sannomiya, S. Nishiyama, S. Ohta, et al., Addit. Manufact. 24 (2018) 498–507, doi:10.1016/j.addma.2018. 10.026
- [30] X. Tong, G. Wu, M.A. Easton, M. Sun, Q. Wang, L. Zhang, Addit. Manufact. 67 (2023) 103487, doi:10.1016/j.addma.2023.103487.
- [31] X. Li, X. Fang, D. Fang, W. Fu, X. Zhang, K. Huang, Addit. Manufact. 77 (2023) 103794, doi:10.1016/j.addma.2023.103794.
- [32] Q. Cao, C. Zeng, X. Cai, R. Zhang, F. Wang, H. Wang, et al., Addit. Manufact. 76 (2023) 103789, doi:10.1016/j.addma.2023.103789.
- [33] C. Shen, Y. Tu, X. Cheng, Z. Li, Y. Jiang, F. Cheng, et al., J. Alloys Compd. 986 (2024) 174063, doi:10.1016/j.jallcom.2024.174063.
- [34] D. Ma, C. Xu, S. Sui, J. Tian, C. Guo, X. Wu, et al., Virtual Phys. Prototyp. 18 (2023) e2225492, doi:10.1080/17452759.2023.2225492.
- [35] Q. Cao, C. Zeng, B. Qi, Z. Jiang, R. Zhang, F. Wang, et al., Addit. Manufact. 67 (2023) 103498, doi:10.1016/j.addma.2023.103498.
- [36] J.J. Bhattacharyya, S.R. Agnew, G. Muralidharan, Acta. Mater. 86 (2015) 80–94, doi:10.1016/j.actamat.2014.12.009.
- [37] W. Yang, H. Yang, K. Yang, X. Lin, Virtual Phys. Prototyp. 19 (2024) e2386592, doi:10.1080/17452759.2024.2386592.
- [38] D. Ma, C. Xu, Y. Qi, S. Sui, J. Tian, T. Tu, et al., J. Mater. Res. Tech. 27 (2023) 6974–6983, doi:10.1016/j.jmrt.2023.11.142.
- [39] Z. Wang, J. Wang, X. Lin, L. Feng, L. Ouyang, C. Dai, et al., J. Mater. Res. Tech. 31 (2024) 1896–1911, doi:10.1016/j.jmrt.2024.06.202.
- [40] F. Chen, X. Cai, B. Dong, S. Lin, J. Mater. Res. Tech. 27 (2023) 2089– 2101, doi:10.1016/j.jmrt.2023.10.063.

- [41] J. Zhan, G. Wu, X. Tong, F. Qi, Q. Wang, R. Jiang, et al., J. Magnes. Alloys (2024), doi:10.1016/j.jma.2024.01.027.
- [42] X. Yang, J. Liu, Z. Wang, X. Lin, F. Liu, W. Huang, et al., Mater. Sci. Engineer.: A 774 (2020) 138942, doi:10.1016/j.msea.2020.138942.
- [43] T. Ying, Z. Zhao, P. Yan, J. Wang, X. Zeng, Mater. Lett. 307 (2022) 131014, doi:10.1016/j.matlet.2021.131014.
- [44] X. Cai, F. Chen, B. Dong, S. Lin, C. Yang, J. Magnes. Alloys (2022), doi:10.1016/j.jma.2022.11.018.
- [45] D.W. Wang, Y.H. Zhou, X.Y. Yao, Y.P. Dong, S.H. Feng, Z.Y. Liu, et al., Mater. Sci. Engineer.: A 832 (2022) 142311, doi:10.1016/j.msea. 2021.142311.
- [46] Z. Wang, J. Wang, X. Lin, L. Feng, L. Ouyang, T. Zhang, et al., J. Mater. Res. Tech. 29 (2024) 4881–4894, doi:10.1016/j.jmrt.2024.02.172.
- [47] W.Z. Wang, D. Wu, R.S. Chen, Y. Qi, H.Q. Ye, Z.Q. Yang, J. Alloys Compd. 832 (2020) 155016, doi:10.1016/j.jallcom.2020.155016.
- [48] J. Zheng, Z. Li, L. Tan, X. Xu, R. Luo, B. Chen, Mater. Charact. 117 (2016) 76–83, doi:10.1016/j.matchar.2016.04.015.
- [49] Y.H. Liu, Z.R. Zhang, J. Wang, Y. Li, H.X. Li, L.Y. Jia, et al., J. Magnes. Alloys 11 (2023) 720–734, doi:10.1016/j.jma.2022.05.012.
- [50] S. Ma, B. Zhao, S. Pan, X. Shen, Y. Yin, Mater. Sci. Engineer.: A 925 (2025) 147856, doi:10.1016/j.msea.2025.147856.
- [51] X. Li, W. Qi, K. Zheng, N. Zhou, J. Magnes. Alloys 1 (2013) 54–63, doi:10.1016/j.jma.2013.02.006.
- [52] B. Li, B.-G. Teng, D-G. Luo, Acta. Metall. Sin (Engl. Lett.) 31 (2018) 1009–1018, doi:10.1007/s40195-018-0769-6.
- [53] M. Calcagnotto, D. Ponge, E. Demir, D. Raabe, Mater. Sci. Engineer.: A 527 (2010) 2738–2746, doi:10.1016/j.msea.2010.01.004.
- [54] Z.F. He, N. Jia, D. Ma, H.L. Yan, Z.M. Li, D. Raabe, Mater. Sci. Engineer: A 759 (2019) 437–447, doi:10.1016/j.msea.2019.05.057.
- [55] P. Luo, D.T. McDonald, W. Xu, S. Palanisamy, M.S. Dargusch, K. Xia, Sci. Mater. 66 (2012) 785–788, doi:10.1016/j.scriptamat.2012.02.008.
- [56] H. Pan, R. Kang, J. Li, H. Xie, Z. Zeng, Q. Huang, et al., Acta. Mater. 186 (2020) 278–290, doi:10.1016/j.actamat.2020.01.017.
- [57] W.T. Sun, X.G. Qiao, M.Y. Zheng, C. Xu, N. Gao, M.J. Starink, Mater. Des. 135 (2017) 366–376, doi:10.1016/j.matdes.2017.09.048.
- [58] J.-F. Nie, Metall. Mater. Trans. A 43 (2012) 3891–3939, doi:10.1007/ s11661-012-1217-2.
- [59] Q. Luo, Y. Guo, B. Liu, Y. Feng, J. Zhang, Q. Li, et al., J. Mater. Sci. Tech. 44 (2020) 171–190, doi:10.1016/j.jmst.2020.01.022.
- [60] X. Gao, S.M. He, X.Q. Zeng, L.M. Peng, W.J. Ding, J.F. Nie, Mater. Sci. Engineer.: A 431 (2006) 322–327, doi:10.1016/j.msea.2006.06.018.
- [61] Z. Yang, Z.H. Wang, H.B. Duan, Y.C. Guo, P.H. Gao, J.P. Li, Mater. Sci. Engineer.: A 631 (2015) 160–165, doi:10.1016/j.msea.2015.02.041.
- [62] Y.Z. Ji, A. Issa, T.W. Heo, J.E. Saal, C. Wolverton, L.-Q. Chen, Acta Mater 76 (2014) 259–271, doi:10.1016/j.actamat.2014.05.002.
- [63] B. Lei, C. Wang, B. Jiang, S. Bai, Z. Dong, X. Qian, et al., Mater. Sci. Engineer.: A 861 (2022) 144371, doi:10.1016/j.msea.2022.144371.